Earth, Planets and Space

FULL PAPER Open Access

Temporal evolutions of N_2^+ Meinel (1,2) band near 1.5. μm associated with aurora breakup and their effects on mesopause temperature estimations from OH Meinel (3,1) band

Takanori Nishiyama[1,2*], Makoto Taguchi[3], Hidehiko Suzuki[4], Peter Dalin[5], Yasunobu Ogawa[1,2,6], Urban Brändström[5] and Takeshi Sakanoi[7]

Abstract

We have carried out ground-based NIRAS (Near-InfraRed Aurora and airglow Spectrograph) observations at Syowa station, Antarctic (69.0°S, 39.6°E) and Kiruna (67.8°N, 20.4°E), Sweden for continuous measurements of hydroxyl (OH) rotational temperatures and a precise evaluation of auroral contaminations to OH Meinel (3,1) band. A total of 368-nights observations succeeded for 2 winter seasons, and 3 cases in which N_2^+ Meinel (1,2) band around 1.5 μm was significant were identified. Focusing on two specific cases, detailed spectral characteristics with high temporal resolutions of 30 s are presented. Intensities of N_2^+ band were estimated to be 228 kR and 217 kR just at the moment of the aurora breakup and arc intensification during pseudo breakup, respectively. At a wavelength of $P_1(2)$ line ($\sim$ 1523 nm), N_2^+ emissions were almost equal to or greater than the OH line intensity. On the other hand, at a wavelength of $P_1(4)$ line ($\sim$ 1542 nm), the OH line was not seriously contaminated and still dominant to N_2^+ emissions. Furthermore, we evaluated N_2^+ (1,2) band effects on OH rotational temperature estimations quantitatively for the first time. Auroral contaminations from N_2^+ (1,2) band basically lead negative bias in OH rotational temperature estimated by line-pair-ratio method with $P_1(2)$ and $P_1(4)$ lines in OH (3,1) band. They possibly cause underestimations of OH rotational temperatures up to 40 K. In addition, N_2^+ (1,2) band contaminations were temporally limited to a moment around the aurora breakup. This is consistent with proceeding studies reporting that enhancements of N_2^+ (1,2) band were observed associated with International Brightness Coefficient 2–3 auroras. It is also suggested that the contaminations would be neglected in the polar cap and the sub-auroral zone, where strong aurora intensification is less observed. Further spectroscopic investigations at these wavelengths are needed especially for more precise evaluations of N_2^+ (1,2) band contaminations. For example, simultaneous 2-D imaging observation and spectroscopic measurement with high spectral resolutions for airglow in OH (3,1) band will make great advances in more robust temperature estimations in the auroral zone.

Keywords: Ground-based spectroscopic observations, OH airglow, Aurora, The Mesosphere and Lower Thermosphere, OH rotational temperature, Short wavelength infrared

Introduction

The mesosphere and lower thermosphere (MLT), from 80 to 120 km altitude in the terrestrial atmosphere, is affected not only by general wind circulation and atmospheric waves with various scales but also solar radiation and energetic particle precipitations from the space. It

*Correspondence: nishiyama.takanori@nipr.ac.jp
[1] National Institute of Polar Research, 10-3, Midori-cho, Tachikawa, Tokyo 190-8518, Japan
Full list of author information is available at the end of the article

is important to understand the MLT thermal structure, dynamics, and compositions that are closely connected to the whole atmosphere system. However, the MLT is hardly accessible, and therefore a method of diagnostic is essentially limited to optical/radio remote sensing, except for direct but transit in-situ measurements by sounding rockets.

Hydroxyl (OH) vibration-rotation emission bands, which were discovered by Meinel (1950), is still glowing its importance as a tracer of the dynamics and the long term trends of the MLT. OH airglow intensity and its rotational temperature have been extensively investigated in the past over 60 years, and consequently they are known to have a variability such as 11-year solar cycle, annual, seasonal, 27-day (Pertsev and Perminov 2008; Shapiro et al. 2012; von Savigny 2015), and planetary-scale wave (Espy et al. 2003; French et al. 2011). It is also noted that short-lived OH enhancements due to solar energetic particle (Damiani et al. 2008; Jackman et al. 2011) and sudden stratospheric warming (Damiani et al. 2010) were reported by satellite-borne measurements.

A variety of OH Meinel bands have been observed for the estimation of OH rotational temperatures; (6,2) band (e.g. Pendleton et al. 2000; Sigernes et al. 2003) and (8,3) band (Phillips et al. 2004) were generally used. In addition, a robust method to auroral contaminations using (8,4) band was presented (Suzuki et al. 2009). OH airglow in Meinel (3,1) band around 1.5 μm is characterized as brighter emission lines than other OH bands and less affected by water vapor absorptions. OH rotational temperatures have been estimated from P-branch in OH (3,1) band by Fourier transform spectrometer and Michelson Interferometer (e.g. Dewan et al. 1992; Sivjee and Walterscheid 1994; Mulligan et al. 1995; Espy et al. 2003; Azeem et al. 2007) since the end of 1980s. From the space, temperatures were retrieved from OH (3,1) band limb emissions with near-global coverage and tangential height steps of 3.3 km (von Savigny et al. 2004; von Savigny 2015). Recent advances in indium gallium arsenide (InGaAs) focal plane array allow to measure intensity of OH (3,1) band with high temporal resolutions by 1-D imaging spectrograph (Schmidt et al. 2013) and 2-D imager with narrow full width at half maximum (FWHM) optical filters, which is capable to "map" OH rotational temperature distributions (Pautet et al. 2018).

Aurora emissions in a wavelength of OH (3,1) band are assumed to be negligible or much weaker than those in visible subrange (Azeem et al. 2007; Pautet et al. 2014), meanwhile, their contribution was not discussed quantitatively so far. Spectroscopic surveys for auroral spectrum in near and short-wavelength infrared regions ($\sim$ 1.6μm) have already been done in the 1970s (e.g. Gattinger and Jones 1973; Jones and Gattinger 1976; Gattinger and Jones 1981; Espy et al. 1987), and many auroral emissions were found such as N_2^+, Meinel (1,2) band around 1.5 μm (Gattinger and Jones 1973). In this paper, detailed spectral characteristics in OH Meinel (3,1) band and N_2^+ Meinel band are presented based on ground-based observations of Near-InfraRed Aurora and airglow Spectrograph, hereafter NIRAS. We also quantitatively evaluate auroral contaminations to OH (3,1) band and discuss about their effects on OH rotational temperature estimations.

Observations

General description

NIRAS is a narrow field imaging spectrograph with a 320 mm focal length and a medium spectral resolution. Figure 1 shows a photo of the NIRAS system in a laboratory for sensitivity calibrations. Main scientific purposes of the NIRAS are as follows: an updating spectral features and absolute intensities in near infrared-short wavelength infrared aurora (0.9–1.6 μm), a precise evaluation of auroral contaminations to OH Meinel (3,1) band, and continuous measurements of OH rotational temperatures. The NIRAS has been installed at Syowa station, Antarctic (69.0°S, 39.6°E) by 59th Japanese Antarctic Research Expedition (JARE) in February 2018. NIRAS observations at Syowa were carried out in an austral winter season, and spectral measurements for a total of 235 nights succeeded. After the operation at Syowa by JARE, the NIRAS was moved and installed again at an optical laboratory in the Swedish Institute of Space Physics (Institutet för rymdfysik, IRF), Kiruna (67.8°N, 20.4°E) in late August 2019. The NIRAS operation at Kiruna focused on OH (3,1) band measurements and monitoring of arctic mesopause temperatures. However, the operation was unfortunately stopped

Fig. 1 A photo of the NIRAS system in a laboratory

in mid-January 2020 due to a trouble in a detector. A history of the NIRAS observations is summarized in Table 1.

Instrument

The NIRAS mainly consists of a Czerny-Turner type spectrometer (HORIBA, iHR320), collecting optics, a detector and a control system. The spectrometer has an entrance slit, a shutter, two mirrors and diffractive gratings (up to three) in a rotating turret. We mainly used two gratings with of groove density of 600 lines per mm (lpmm) and 150 lpmm, which correspond to spectral sampling of 0.11 nm/pixel and 0.50 nm/pixel, respectively. The gratings can be switched remotely via software. The collecting optics, mounted in front of a slit, are a gold coated off-axis parabolic mirror and a long-pass filter for removal of secondary diffracted light in visible wavelength. The detector is 1-D InGaAs array (HORIBA, Symphony IGA) that has thermoelectric cooling system (about −50°C) and 1024 pixels with a pixel size of 25 μm × 250 μm. It has a sensitivity to light from 0.8 to 1.7 μm at a room temperature. Since clarifying absolute intensity of aurora emissions from 0.9 to 1.6 μm is one of main subjects, the NIRAS sensitivity has been calibrated before transportation to Syowa. For the calibration, a 12-inch integrating half-sphere, a Kr lamp, and two different multi-channel spectrometers with Charge Coupled Device (CCD, 360–1100 nm) and InGaAs (900–1600 nm) were used. Continuum and spatially uniform light can be made by the half-sphere and the lamp, and the NIRAS and the multi-channel spectrometers, which are capable of measuring the absolute light intensity between 360 and 1600 nm, simultaneously measured the light from an open port of the half-sphere. Based on the calibration, we confirmed that the NIRAS with both of the two gratings had an enough sensitivity for airglow and aurora emissions from 0.9 to 1.6 μm. The detailed specifications of the NIRAS are presented in Table 2. The NIRAS was operated automatically when Solar Zenith Angle (SZA) is greater than 100° at Syowa and 96° at Kiruna, according to a provided schedule, and ran routinely regardless of moon phases and meteorological conditions.

Results

OH 3,1 band measurements and temperature estimations

Typical nightly mean spectrum obtained from NIRAS measurements on May 29 and May 6, 2018 are shown in Fig. 2; Fig. 2 a is a spectra with the 600-lpmm grating and a center wavelength of 1504 nm. Q- and P-branches in OH (3,1) band are from 1500 to 1555 nm in the spectra. On the other hands, Fig. 2 b is a spectra with the 150-lpmm grating and a center wavelength of 1371 nm. Q-branches in OH (6,3), (7,4), (8,5), (2,0), (3,1), and (4,2) bands and O_2 ($^1\Delta$) band are identified. Water vapor absorptions, which are significant from 1350 to 1450 nm in lower latitudes, seem to be not serious, although no emissions are found from 1350 to 1400 nm in the spectra. It should be noted that data near the edge on a short wavelength side is not reliable due to low sensitivity of the NIRAS and water vapor absorption, and therefore not used for quantitative discussions.

Figure 3 is a summary plot for the NIRAS observations in austral winter 2018 that only shows nightly means of spectral measurements for OH (3,1) band. Results obtained by measurements with the 600-lpmm grating are only shown. Figure 3a is total exposure time for nightly mean OH (3,1) band intensities and temperature on each night. We only used good Signal-to-Noise Ratio (SNR) spectral data for calculating the nightly mean. Criteria are as follows: SNR of $P_1(2)$ and $P_1(4)$ line intensities are greater than 1.3 and 1.0 before March 24, 2018 because focus of the NIRAS was not fully adjusted yet. After focus adjustment on March 24, 2018, the criteria are changed to SNR of 2.0 and 1.6. Zero exposure time means either no good SNR data mainly due to meteorological conditions or running in different target modes. A dashed curve indicates amount of time when SZA is greater than 100 degrees on each night. Note that the time is multiplied by a factor of 5/6 because a cycle of measurement has one dark frame and five sky frames. As shown in Fig. 3a, continuous measurements with good SNR were done from the middle to the end of May 2018.

Figure 3b shows seasonal variability of nightly mean of $P_1(2)$, $P_1(3)$, and $P_1(4)$ line intensities in OH (3,1)

Table 1 A summary of locations and period for NIRAS observations

	Syowa Station, Antarctic	IRF, Sweden
Location	69.0°S, 39.6°E (Magnetic latitude: 66.9°S)	67.8°N, 20.4°E (Magnetic latitude: 65.2°N)
Period	March 7–November 2, 2018 (austral winter)	August 28, 2019–January 10, 2020
# of observations	235 nights (168 nights, a 600-lpmm grating for OH (3,1) band)	133 nights (127 nights, a 600-lpmm grating for OH (3,1) band)

Table 2 Key properties of the NIRAS, both the spectrometer and the detector are manufactured by HORIBA Scientific. Typical operational parameters are also shown

Specifications of the NIRAS		
Spectrometer	Czerny-Turner	
Focal length	320 mm	
F number	4.1	
Slit width	0.10 mm (0–2 mm, electrically controlled)	
Etendue	0.014–0.017 cm^{2}*sr	
Field-of-view	0.019° × 0.19°	
Detector	InGaAs 1-D array	
Pixel size	25 µm × 250 µm (W × H)	
Number of pixel	1024	
Operation temperature	−52.0 ± 0.2 °C, thermoelectric cooling	
Grating	600 lpmm	150 lpmm
Blaze wavelength	1500 nm	1200 nm
Spectral sampling	0.11 nm/pixel	0.50 nm/pixel
Spectral resolution	≥ 0.42 nm	≥ 1.9 nm
Spectral range	119 nm	510 nm

Observation setting of the NIRAS	
Observation condition	Syowa: SZA ≥ 100°, Kiruna: SZA ≥ 96°
Center of field-of-view	Syowa: local magnetic zenith (63.4°), Kiruna: local zenith
Temporal resolution	30 s (exposure 29 s)
Data acquisition cycle	3 min: 1 dark frame and 5 sky frames
Airglow target	OH Meinel (3,1) band with the 600-lpmm grating
Aurora target	N_2^+ Meinel band and N_2 1st positive band with the 150-lpmm grating

band. Basically the intensity seems to have no clear periodical fluctuations, but significant enhancements can be seen a few times in May 2018. Figure 3c is nightly mean of OH rotational temperatures that was estimated based on line-pair-ratio method using a ratio between $P_1(2)$ and $P_1(4)$ line intensities (e.g. Meriwether 1975; Pautet et al. 2014). Rotational term values and Einstein coefficients are referred from Krassovsky et al. (1962) and Mies (1974), respectively. The nightly mean and 3-days smoothing are indicated by black diamonds and red lines, respectively. A blue curve is seasonal variations of temperature at 87-km altitude, which is widely accepted as a center of OH emission layer (Baker and Stair 1988), calculated by NRLMSISE-00 (Picone et al. 2002). In addition, green triangles are 3-day smoothed temperature at geopotential height of 80 km obtained from Aura/Microwave Limb Sounder (MLS). Tangential points of all MLS data are within 69.0° ± 2°S latitude and 39.6° ± 3.0°E longitude. The estimated temperature by the NIRAS measurements of OH (3,1) band is well correlated to that by Aura/MLS measurements. MLS temperature at geopotential height of 80 km was the best among other geopotential heights. This is consistent with that a peak height of OH for vibrational number of 6, which should be 1km higher than OH layer for vibrational number of 3 observed by the NIRAS (von Savigny et al. 2012), ranges from 79 to 82 km at 71°S in austral winter (Grygalashvyly et al. 2014).

The NIRAS successfully resolved nocturnal variations in OH (3,1) band as well as day-to-day variations. Figure 4 is a summary plot for NIRAS measurement on May 29, 2018. Figure 4a is SZA, and the NIRAS observation ran about 16 hours when SZA was greater than 100° on this night. In Fig. 4b, a black and a red lines show temporal variations in sensor temperature in every 30 s and in 3-min average, respectively. Sensor temperature, which is a proxy of data quality, was stable around −52°C with standard deviations of $0.22°C$. Figure 4c is geomagnetic field variation in H, D, Z-components observed by a fluxgate magnetometer and it shows that geomagnetic activity was quiet throughout the night. Figure 4d shows dynamic spectrum with a wavelength coverage from 1451 to 1557 nm and a temporal resolution of 3 min. Q- and P-branches in OH (3,1) band are clearly seen in a wavelength longer than 1500 nm. $P_1(2)$, $P_1(3)$, and $P_1(4)$ line intensities as a function of time are shown in Fig. 4e. Figure 4f is estimated OH rotational temperatures

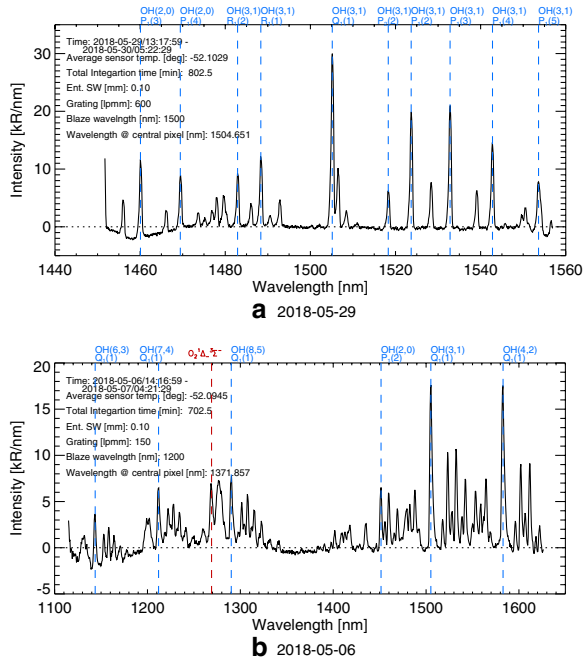

Fig. 2 Typical nightly mean spectrum obtained from NIRAS measurements on May 29 and May 6, 2018. **a** A spectra with the 600-lpmm grating and a center wavelength of 1504 nm. **b** A spectra with the 150-lpmm grating and a center wavelength of 1371 nm. It should be noted that data near the edge on a short wavelength side is not reliable, and therefore not used for quantitative discussions

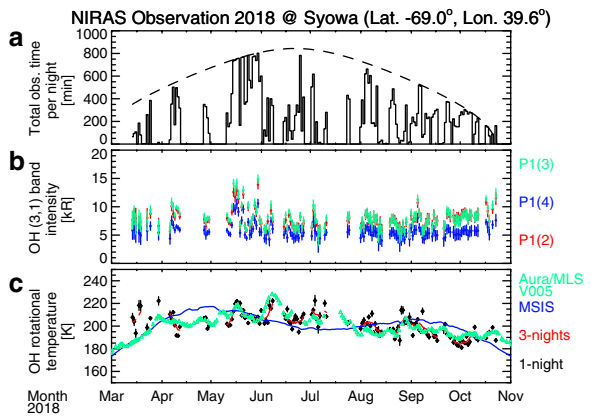

Fig. 3 NIRAS spectral measurements of OH Meinel (3,1) band at Syowa station in 2018 austral winter. Results obtained by measurements with the 600-lpmm grating are only shown. **a** Total exposure time for nightly mean intensities and temperature on each night. We only used good SNR data for the mean and a detail is described in a main text. A dashed curve indicates amount of time when SZA is greater than 100 ° on each night. Note that the time is multiplied by a factor of 5/6 because a cycle of measurement has one dark frame and five sky frames. **b** Nightly mean of $P_1(2)$, $P_1(3)$, and $P_1(4)$ line intensities in OH (3,1) band. **c** Nightly mean of OH rotational temperatures estimated by a ratio between $P_1(2)$, and $P_1(4)$ line intensities. The nightly mean and 3-days smoothing are indicated by black diamonds and red lines, respectively. A blue curve is seasonal variations of 3-day smoothed temperature at 87-km altitude calculated by NRLMSISE-00 (Picone et al. 2002). Green triangles are 3-day smoothed temperature at geopotential height of 80 km obtained from Aura/MLS

in every 3 min (black diamonds) and 30-min smoothed temperatures (red line). Errors of estimated temperatures are mostly less than 4 K in this case. Figure 4g is same as f but 15-min averaged temperatures by the same error-weighted scheme as in Schmidt et al. (2013) (black diamonds) and 60-min smoothed temperatures (red line). Temperature variations with long-periods (longer than a few hours) can be identified as well as those with short-periods (shorter than 1 h).

Auroral contamination to OH (3,1) band

We present two cases in which OH (3,1) band was contaminated by N_2^+ Meinel (1,2) aurora band. Figure 5 is a first case of NIRAS measurements with the 150-lpmm grating on May 6, 2018 and comparisons to observed aurora activity. Figure 5a is geomagnetic field variations in H, D, and Z components showing a rapid depletion (~ -900 nT) in H component at 22:10 UT. Figure 5b and c are keograms along magnetic latitudinal directions obtained from co-located all-sky aurora imagers for N_2^+ 427.8 nm and O 557.7 nm, respectively. These indicate that aurora breakup took place at the same time as the H-component depletion. Figure 5d is aurora intensity of O 557.7 nm at magnetic zenith as a function of time. The intensity of O 557.7 nm reached ~ 200 kR (N_2^+ 427.8 nm ~ 100 kR, not shown), which indicated strong aurora intensification. Figure 5e is dynamic spectrum from 1114 to 1624 nm obtained by the NIRAS. At the beginning of the observation, a strong enhancement of O_2 ($^1\Delta$) band at 1270-1280 nm in twilight conditions was observed. Q-branches in OH (3,1) and (4,2) bands around 1500 nm and 1580 nm can be identified throughout the night. At the moment of the aurora breakup, N_2 1st positive (0,1) band was noticeable at 1220-1240 nm. At the same time faint emissions from 1450 to 1540 nm, corresponding to N_2^+ Meinel (0,1) and (1,2) bands, were overlapped with OH (2,0) and (3,1) bands. $P_1(2)$, $P_1(3)$, and $P_1(4)$ line intensities in OH (3,1) band as a function of time are shown in Fig. 5f. Focusing on a period at the aurora breakup, the intensity in $P_1(2)$ and $P_1(3)$ lines showed spike-like increases up to 10 kR. On the other hand, no clear change was found in $P_1(4)$ line. More detailed spectral features are shown and discussed later.

A second case was NIRAS observation at IRF, Kiruna on September 21, 2019, which is summarized in Fig. 6. Figure 6a is local *K*-index based on geomagnetic field observations at Kiruna. The *K*-index was 5 from 2100

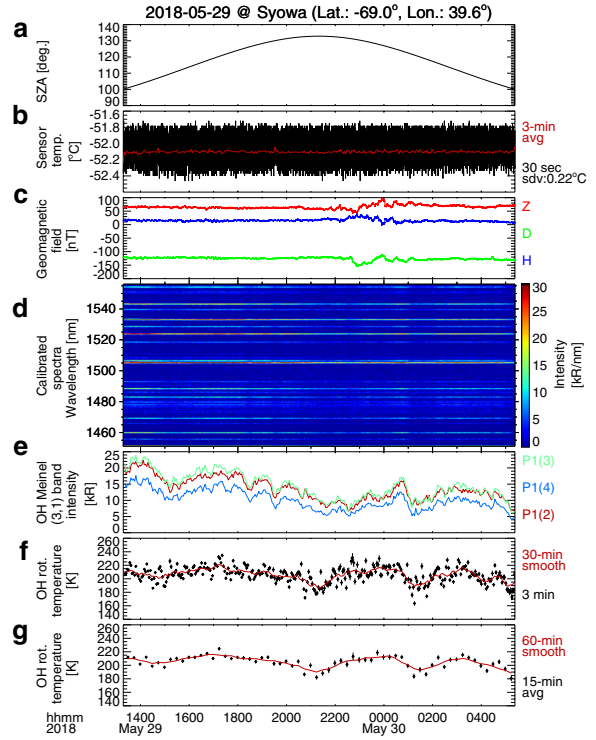

Fig. 4 A summary plot for NIRAS measurements of OH Meinel (3,1) band and estimated OH rotational temperature on May 29, 2018. **a** SZA as a function of time **b** Sensor temperature variations in every 30 s (black) and 3-min average (red) **c** Geomagnetic field variations in H, D, and Z components observed by a fluxgate magnetometer at Syowa **d** Dynamic spectrum from 1451 to 1557 nm obtained by the NIRAS. **e** $P_1(2)$, $P_1(3)$, and $P_1(4)$ line intensities in OH (3,1) band as a function of time. **f** Estimated OH rotational temperatures in every 3 min (black diamonds) and 30-min smoothed temperatures (red line). Errors of estimated temperatures are mostly less than 4 K. **g** Same as (**f**) but 15-min averaged temperatures by error-weighted scheme (black diamonds) and 60-min smoothed temperatures (red line)

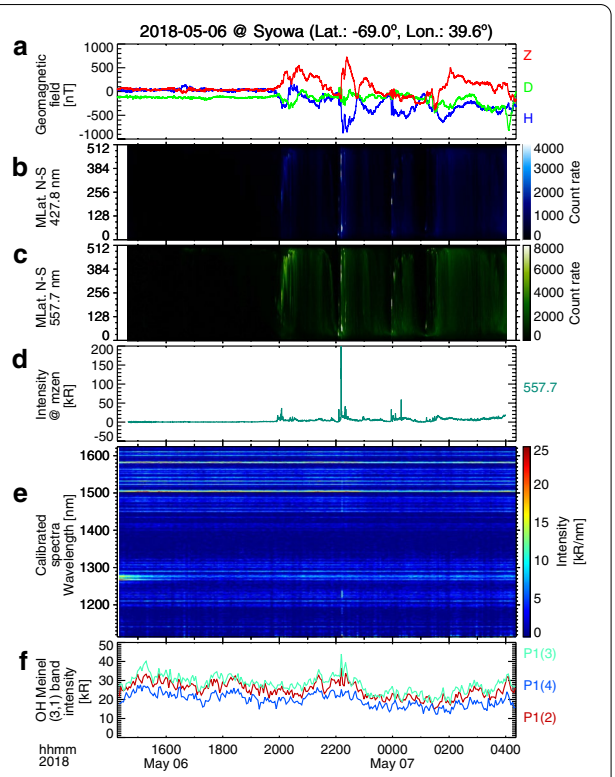

Fig. 5 NIRAS measurements with the 150-lpmm grating on May 6, 2018 and comparisons to observed aurora activity. **a** Geomagnetic field variations in H, D, and Z components (**b**) and **c** Aurora keograms along magnetic latitudinal directions obtained from all-sky aurora imagers for N_2^+ 427.8 nm and O 557.7 nm, respectively **d** Aurora intensity of O 557.7 nm emission at magnetic zenith as a function of time. **e** Dynamic spectrum from 1114 to 1624 nm obtained by the NIRAS. **f** $P_1(2)$, $P_1(3)$, and $P_1(4)$ line intensities in OH (3,1) band as a function of time

to 2400 UT indicating geomagnetically active condition. Figure 6b and c are keograms along geomagnetic north–south and east–west directions, respectively, and the both are from Watec monochromatic imager for wavelength of 557.7 nm (Ogawa et al. 2020). The keograms indicate that isolated east–west aligned arc localized near zenith was gradually intensified and another arc in a higher latitude was moving equatorward until 2150 UT. Finally, the two arc were merged near zenith and further intensified at 2154 UT. However, this activity neither expanded over the whole sky nor reached full breakup later, and therefore it seems a pseudo breakup typically seen in pre-midnight (Partamies et al. 2003). Aurora intensity at a geographic zenith in Fig. 6d also shows drastic variations after 2130 UT and a rapid enhancement near 2150 UT. We cannot follow the intensity variations between 2150 and 2200 UT due to CCD saturations, however, it suggests that the intensified arc was stable for about 10 min. All-sky aurora image data at Sodankylä Geophysical Observatory (67.4°N, 26.4°E, Magnetic latitude: 64.1°), Finland also demonstrates the intensification of aurora arc and pseudo breakup at that moment (See Additional file 1: Video S1 in more detail). The NIRAS was likely to observe the same intensified arc as that observed at wavelength of 557.7 nm. In fact, strong auroral emissions in N_2 1st positive (0,1) band, N_2^+ Meinel (0,1) and (1,2) bands are clearly seen from 2152 to 2155 UT in dynamic spectrum of Fig. 6e. Figure 6f is intensity of $P_1(2)$, $P_1(3)$, and $P_1(4)$ lines in OH (3,1) band as a function of time. It should be noted that increases in the intensity caused by N_2^+ auroral contaminations are obvious at each line.

Detailed spectral analysis

Next, we present more detailed analysis to observed spectrum in the two cases. Figure 7 shows observed

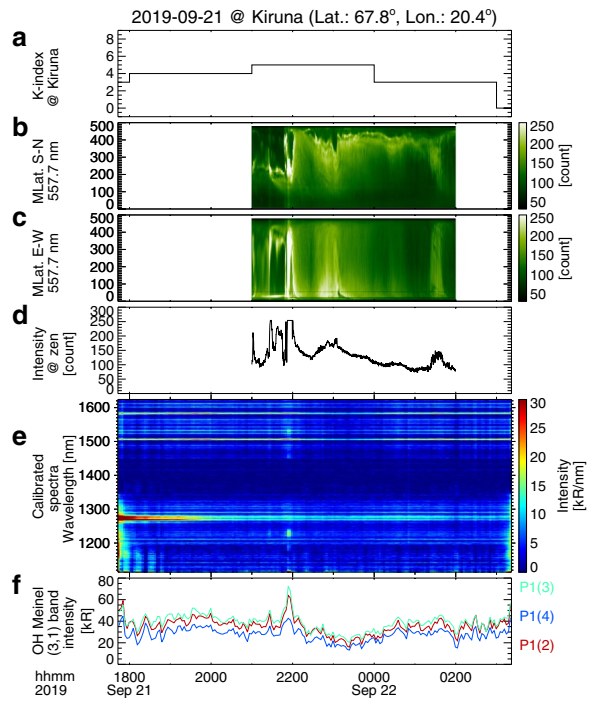

Fig. 6 NIRAS measurements with the 150-lpmm grating at IRF, Kiruna on September 21, 2019. **a** Local *K*-index obtained from geomagnetic field observations at Kiruna. **b** and **c** are keograms along geomagnetic north–south and east–west directions, respectively. **d** Auroral intensity at a geographic zenith as a function of time **e** Dynamic spectrum from 1114 to 1624 nm obtained by the NIRAS. **f** $P_1(2)$, $P_1(3)$, and $P_1(4)$ line intensities in OH (3,1) band as a function of time

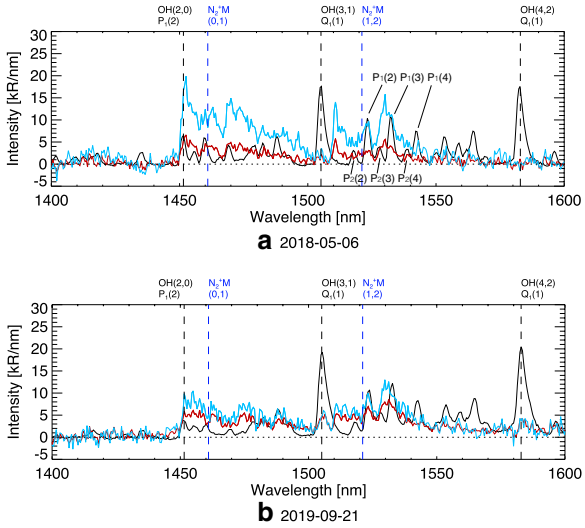

Fig. 7 Spectrum in a wavelength range from 1400 to 1600 nm obtained **a** at Syowa station, on May 6, 2018 and **b** at IRF on September 21, 2019. A black solid line is nightly mean spectrum, and therefore OH airglow emissions are thought to be dominant. Red and blue lines are spectrum observed at aurora breakup with time resolutions of 3 min (2210:00 UT on May 6, 2018 and 2152:00 UT on September 21, 2019) and 30 s (2211:00 UT on May 6, 2018 and 2154:30 UT on September 21, 2019), respectively

spectrum in a wavelength range from 1400 to 1600 nm; black lines are nightly mean spectrum, and therefore OH airglow contributions to the spectrum are thought to be dominant. On the other hand, red and blue lines are nominal aurora spectrum that were obtained from subtracting the nightly mean from the observed spectrum at active aurora periods (e.g. Gattinger and Jones 1973; Espy et al. 1987). Time resolutions of those spectrum are 3 min (1 cycle, red) and 30 s (1 sky frame, blue), respectively. This analysis assumes that the OH spectrum at the time of the auroral breakups were the same as the nightly mean spectrum. However, the OH emission intensity should vary during nights. Actually, intensity in $P_1(2)$ and $P_1(4)$ lines in OH (3,1) band varied with amplitudes of about 10–20 kR in the two nights as shown in Figs. 5f and 6f. We have checked hourly mean OH (3,1) band spectrum just before the auroral intensification in the two events. Spectral intensity differences between the nightly means and the hourly means are less than 2 kR/nm, and they typically range from 0.3 to 0.5 kR/nm in 1510–1550 nm. This suggests that these differences are thought to be insignificant to spectral shapes of N_2^+ (1,2) Meinel band leading to auroral contaminations in OH (3,1) band in the presented cases. Figure 7a are nightly mean spectra and nominal aurora spectrum with different time windows (from 2210 to 2213 UT and from 2211:00 to 2211:30 UT) on May 6, 2018. They demonstrate that OH (3,1) band, mainly $P_2(2)$, $P_1(2)$, $P_2(3)$, $P_1(3)$, $P_2(4)$, and $P_1(4)$, was spectrally overlapped with N_2^+ (1,2) band. Intensity of the band, which is integrated in a wavelength from 1508 to 1540 nm, was 79.5 kR in 3-min average (2.5-min exposures). In 30-s resolution data, the intensity was estimated to be 228 kR just at the moment of the aurora breakup, which causes severe contaminations to OH (3,1) band and subsequently leads significant errors of OH rotational temperatures. In particular, intensity of $P_1(2)$ and $P_1(3)$ lines were almost the same or less than that of N_2^+ (1,2) band.

Figure 7b is the same plot as Fig. 7a but obtained on September 21, 2019. Nominal aurora spectrum indicated by red and blue lines are corresponding to time windows from 2152 to 2155 UT and from 2154:30 to 2155:00 UT, respectively. In a comparison to the previous case, a spectral shape of N_2^+ (1,2) band seems to be not well-defined. This is partly because focus adjustment was not completely done. The estimated intensities in 3 min and 30 s resolutions were 160 kR and 217 kR, respectively. The two intensities in different time resolutions are not so different, which suggests that the aurora arc did not change

spatially and temporally for a few minutes. N_2^+ auroral contaminations to OH (3,1) band were also not negligible in this case.

We made further analysis to evaluate quantitatively N_2^+ aurora effects on OH rotational temperature measurements. Figure 8 shows summary plots of the analysis for the spectral data observed (a) at Syowa station, on May 6, 2018 and (b) at Kiruna on September 21, 2019. Top plots in Fig. 8 show the nightly mean of observed spectrum (black) and artificial spectrum (red) that are created from convolutions of numerically simulated OH (3,1) band spectrum ($P_1(2)$, $P_1(3)$, $P_1(4)$, $P_2(2)$, $P_2(3)$, and $P_2(4)$) and NIRAS instrumental functions. Temperatures estimated from the nightly mean were used for the spectrum calculations. Although FWHMs of the NIRAS were different between Syowa and Kiruna, the theoretically reproduced spectrum of OH (3,1) band were well agreed to the both observed ones. In middle plots of Fig. 8 red and blue lines are the reproduced OH airglow spectrum and the observed N_2^+ (1,2) aurora spectrum with 30-s resolutions that were already shown in Fig. 7, respectively. Black lines are synthetic spectrum that were obtained by the OH airglow spectrum plus the N_2^+ aurora spectrum. Peaks corresponding to $P_1(2)$, $P_1(3)$, and $P_1(4)$ lines in OH (3,1) band were still seen in the synthetic spectrum. But $P_2(2)$, $P_2(3)$, and $P_2(4)$ lines were difficult to be identified. Bottom plots in Fig. 8 show a ratio between OH airglow intensity and total intensity (OH airglow and N_2^+ (1,2)) as a function of wavelength. If the ratio is close to zero, N_2^+ auroral contaminations are dominant, and therefore it is difficult to assume pure OH airglow spectrum anymore. It should be noted that N_2^+ aurora contributions were not uniformly distributed in OH (3,1) band in the both cases; the aurora contributions around $P_1(2)$ lines in OH (3,1) band were large, on the other hand those around $P_1(4)$ lines in OH (3,1) band were relatively small. This dependence on wavelength is expected to lead negative bias in estimated temperature, because a volume emission rate

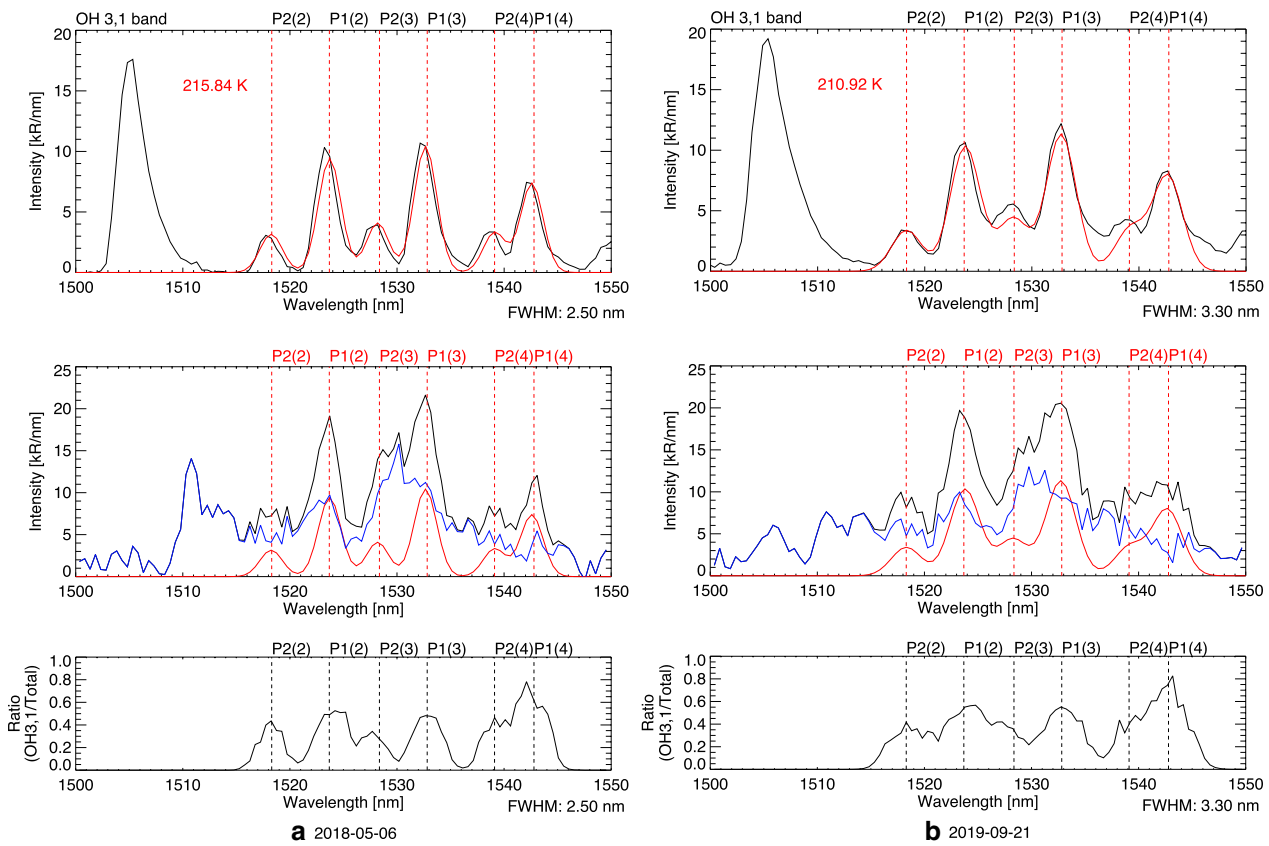

Fig. 8 Summary plots for evaluating N_2^+ Meinel (1,2) auroral contaminations to OH (3,1) band measurements based on spectral data **a** at Syowa station, on May 6, 2018 and **b** at Kiruna on September 21, 2019. (Top) The nightly mean spectrum (black) and artificial spectrum (red) that are created from convolutions of OH (3,1) band spectrum ($P_1(2)$, $P_1(3)$, $P_1(4)$, $P_2(2)$, $P_2(3)$, and $P_2(4)$) and instrumental functions. (Middle) Red and blue lines are the artificial OH airglow spectrum and the observed N_2^+ Meinel (1,2) aurora spectrum, respectively. Synthetic spectrum are shown by black lines. (Bottom) Ratio between OH airglow intensity and total intensity (OH airglow and N_2^+ Meinel (1,2)) as a function of wavelength

of $P_1(2)$ line in OH (3,1) band becomes larger at lower temperature due to its negative rotational term values (Krassovsky et al. 1962).

Table 3 summarizes observed spectral characteristics about OH (3,1) and N_2^+ (1,2) bands in the presented events. As already mentioned in the text, aurora morphology in the events were different; the NIRAS observed the spectrum associated with aurora breakup and isolated arc intensification. In addition, FWHM of the NIRAS at Kiruna was by 0.8-nm broader corresponding to spectral band of one pixel. In Table 3, we show the intensity of N_2^+ (2,1) band that is integrated for specific wavelength ranges corresponding to $P_1(2)$ and $P_1(4)$ lines in OH (3,1) band with the FWHMs. For $P_1(2)$ line, intensity ratios between N_2^+ (1,2) and OH (3,1) were 1.4 and 1.1 at Syowa and Kiruna, respectively, and therefore N_2^+ emissions were almost equal to or greater than OH emissions at this wavelength. For $P_1(4)$ line, they were 0.75 and 0.67, which means that OH emissions were contaminated from N_2^+ emissions but still dominant. If we do not take into account these auroral contaminations, OH rotational temperatures in the two cases are estimated to be 178.8 K and 172.0 K, respectively. Since temperatures based on the nightly mean are 215.8 K and 210.9 K, auroral contaminations from N_2^+ (1,2) band possibly cause underestimations of OH rotational temperatures up to 40 K.

We found another case that was associated with aurora breakup taking place at Syowa on March 23, 2018. This case was similar to that at Syowa on May 6, 2018, but a depletion of H-component for the breakup (~ -600 nT) was a little bit smaller than on May 6. Observed aurora emission in N_2^+ (1,2) band was also weaker and its spectral structure was unclear without no well-defined peaks. OH (3,1) band intensity was 2-5 times stronger than N_2^+ (1,2) band around wavelengths of $P_1(2)$ and $P_1(4)$ lines. As a result, negative bias in OH rotational temperature can be smaller and estimated about 8 K.

Discussion and conclusions

We found only three cases, in which aurora emissions in N_2^+ (1,2) band were significant in the NIRAS data, from a total of 368-nights observations at Syowa and Kiruna. Each maximum of *K*-index of the three were 5 or 6, and therefore all cases took place during geomagnetically disturbed but not severe conditions. Among the three, spectral characteristics of N_2^+ (1,2) band were totally different in their intensities and spectral shapes. The two presented cases revealed that N_2^+ (1,2) band was definitely a source of contaminations to OH (3,1) band measurements and cannot be neglected. Furthermore, this contamination has potential to lead underestimations of OH rotational temperature. Due to small number of samples we cannot make a further analysis and discuss about spectral variability of N_2^+ (1,2) band, but it must be taken into account that auroral contaminations from this band and their effects on OH (3,1) band measurements potentially change case by case. Dominant generation process of N_2^+ (1,2) is thought to be direct electron impact on N_2 (Gattinger and Jones 1973), and it is also suggested that $O^+(^2D)$ - N_2 charge transfer process contributes to productions of N_2^+ as auroral source (Omholt 1957). Aurora height significantly affects these processes (Espy et al. 1987), and therefore further observations, for example coordinated with incoherent scatter radars, are needed to clarify temporal variability of N_2 (1,2) band depending on aurora height.

Table 3 A summary of spectral characteristics of OH (3,1) and N_2^+ (1,2) bands for the two aurora events observed by the NIRAS

Event	May 6, 2018 @ Syowa	September 21, 2019 @ Kiruna
Aurora morphology	Aurora breakup	Isolated aurora arc intensification
NIRAS FWHM	2.5 nm	3.3 nm
OH temperature (nightly mean)	215.8 K	210.9 K
Wavelength: $P_1(2)$, *OH (3,1) band*	1521.2–1525.7 nm	1520.8–1526.3 nm
Intensity of OH (3,1) band	24.6 kR	37.1 kR
Intensity of N_2^+ (1,2) band	35.5 kR	41.8 kR
Ratio N_2^+ (1,2) / OH (3,1)	1.4	1.1
Wavelength: $P_1(4)$, *OH (3,1) band*	1540.1–1544.6 nm	1540.7–1545.2 nm
Intensity of OH (3,1) band	21.2 kR	27.3 kR
Intensity of N_2^+ (1,2) band	15.9 kR	18.5 kR
Ratio N_2^+ (1,2) / OH (3,1)	0.75	0.67
Contaminated OH temperature	178.8 K	172.0 K

The presented three cases suggest that enhancements of N_2^+ (1,2) band intensity are closely related to the aurora breakup or the aurora arc intensification. In proceeding studies, N_2^+ (1,2) band was observed with IBC 2-3 auroras (Gattinger and Jones 1973, 1981), and that is consistent with our studies. Since Syowa and Kiruna are located in so-called auroral zones, it is difficult to eliminate the contaminations due to aurora intensification even at a wavelength near 1.5 μm. But, meanwhile, any enhancements of N_2^+ (1,2) band related to aurora arc in pre-onset conditions and active diffuse/pulsating aurora after breakups were not identified by our observations. Thus, N_2^+ (1,2) band contaminations would be temporally limited to a moment around aurora breakup. Since aurora intensity is highly variable in time and basically smoothed out with low temporal resolutions or longer integration time as shown in Fig. 7a, it is noted that OH measurements with high temporal resolutions would suffer from the auroral contaminations seriously. On the other hand, the contaminations are expected to make minor contributions in the polar cap and the sub-auroral zone, where strong aurora intensification related to breakup is less observed directly (Azeem et al. 2007).

The NIRAS mostly ran with the 600-lpmm grating (FWHM: 0.63 nm) and a target of OH (3,1) band. It amounts to 295 (168, Syowa and 127, Kiruna) nights, corresponding to 80% of total observations. However, no aurora emissions were identified in the high spectral resolution data so far, while the NIRAS observation in this setting has been implemented for 88 (56, Syowa and 32, Kiruna) geomagnetically disturbed nights (30%) that are defined as with a maximum *K* index larger than 5. On the other hand, the NIRAS ran with the 150-lpmm grating for only 10 nights (8, Syowa and 2, Kiruna), and 5 nights of them were regarded as geomagnetically disturbed nights. We must consider a possibility that the NIRAS missed temporal and spatial variations of aurora for the other 90 geomagnetically disturbed nights due to its narrow FOV.

One interesting thing is that N_2^+ (1,2) band intensification was only found by NIRAS observations with the 150-lpmm grating. The NIRAS sensitivity has no much differences between the two modes; each sensitivity for photons at 1.5 μm are almost the same. FWHMs of 600- and 150-lpmm are 0.63 nm and 2.5 or 3.3 nm, respectively. Narrow FWHM will allow us to resolve spectral shapes of N_2^+ (1,2) band more clearly, and therefore the difference of FWHMs cannot be the reason why no aurora emissions were identified around 1.5 μm with the 600-lpmm grating. Further spectroscopic investigations at this wavelength are needed especially for more precise evaluations of N_2^+ (1,2) band contaminations, since a highly resolved spectral data helps us to avoid the auroral contaminations to OH (3,1) band. Based on our results, it can be concluded that spectral resolutions of a few nm FWHM are difficult to avoid the auroral contaminations. But we should also note that our calculations of temperature estimation errors ($\sim$ 40 K) are applicable to OH measurements with a few nm spectral resolutions. FWHM less than 1 nm will make better and robust temperature estimations in spite of N_2^+ (1,2) band contaminations. Moreover, a wider field-of-view is preferable for getting more chances to coincident detections of aurora and airglow emissions. In the next step, simultaneous 2-D imaging observation and spectroscopic measurement with high spectral resolution for airglow in OH (3,1) band will make great advances in more precise evaluations of auroral N_2^+ (1,2) contaminations and subsequent robust temperature estimations in the auroral zone.

We presented detailed spectral characteristics of short wavelength infrared aurora and airglow around 1.5 μm by the NIRAS measurements with high temporal resolutions of 30 s based on the two specific cases. Furthermore, we evaluated N_2^+ (1,2) band effects on OH (3,1) band measurements quantitatively for the first time. This study can be summarized as follows.

(1) We have carried out NIRAS observations at Syowa (from March 7, 2018 to November 2, 2018) and Kiruna (from August 28, 2019 to January 10, 2020). A total of 368-nights observations succeeded for two seasons.
(2) Only three cases in which aurora emissions in N_2^+ (1,2) band were significant in the NIRAS data were found. *K*-index of the three were 5 or 6, and therefore all cases took place during geomagnetically disturbed but not severe conditions.
(3) The two specific cases demonstrated that OH (3,1) band, mainly $P_2(2)$, $P_1(2)$, $P_2(3)$, $P_1(3)$, $P_2(4)$, and $P_1(4)$, was spectrally overlapped with N_2^+ (1,2) band. Intensities of N_2^+ band were estimated to be 228 kR and 217 kR in 30-s resolutions just at the moment of the aurora breakup and the arc intensification during the pseudo breakup, respectively.
(4) At a wavelength of $P_1(2)$ line ($\sim$ 1523 nm), N_2^+ emissions were almost equal to or greater than the OH line intensity. On the other hand, at a wavelength of $P_1(4)$ line ($\sim$ 1542 nm), the OH line was not seriously contaminated and still dominant to N_2^+ emissions. This basically leads to negative bias in estimated OH rotational temperature by line-pair-ratio method with $P_1(2)$ and $P_1(4)$ lines. They possibly cause underestimations of OH rotational temperatures up to 40 K.

(5) N_2^+ (1,2) band contaminations were temporally limited to a moment around the aurora breakup. This result suggests that the contaminations would be neglected in the polar cap and the sub-auroral zone, where strong aurora intensification comparable to IBC 2–3 is less observed.
(6) Further spectroscopic investigations at this wavelength are needed. For example, simultaneous 2-D imaging observation and spectroscopic measurement with high spectral resolution for airglow in OH (3,1) band will make great advances in more precise evaluations of auroral N_2^+ (1,2) contaminations and consequently robust temperature estimations in the auroral zone.

Supplementary Information

The online version contains supplementary material available at https://doi.org/10.1186/s40623-021-01360-0.

Additional file 1: Video S1. A aurora movie at Sodankylä Geophysical Observatory for a night on September 21, 2019. This movie is from images captured by an intensified CCD all-sky camera with 512 × 512 pixels and the image intensifier. The single frame exposure is 600 milliseconds for a wavelength of 557.7 nm and it repeated every 20 s. In the movie, strong intensification of aurora arc can be seen at 2154:20 UT, which are probably the same as those observed at Kiruna.

Acknowledgements
This work was supported by Japan Society for the Promotion of Science (JSPS), Grants-in-Aid for Young Scientists (A) 17H04857 and Scientific Research (B), Shimadzu Science Foundation, the prioritized project AJ0901 of Japanese Antarctic Research Expedition, and the Project Research KP301 of the National Institute of Polar Research. Magnetic field data and all-sky aurora image data at Syowa were provided by National Institute of Polar Research, Japan. The Upper Atmosphere Physics Monitoring Observation at Syowa Station was mainly supported by the Research Program of Japanese Antarctic Research Expedition (JARE) of the Ministry of Education, Culture, Sports, Science, and Technology of Japan (MEXT). All-sky imager at Kiruna data was provided by National Institute of Polar Research, Japan. The distribution of the magnetic field data has been partly supported by the IUGONET (Inter-university Upper atmosphere Global Observation NETwork) project (http://www.iugonet.org/) funded by the MEXT. *K*-index data at Kiruna is produced by The Swedish Institute of Space Physics, Kiruna. We appreciate for making the *K*-index dataset available. All-sky camera data at Sodankylä is produced by Sodankylä Geophysical Observatory, University of Oulu. A timelapse movie is created by Dr. T. Raita, Sodankylä Geophysical Observatory, University of Oulu. We thank the NASA Goddard Earth Sciences (GES) Data and Information Services Center (DISC) (https://disc.gsfc.nasa.gov/) for providing the Aura/MLS temperature and geopotential height dataset.

Authors' contributions
TN (corr-auth) designed this research, operated NIRAS at Syowa on site and Kiruna via internet, led data analysis, and wrote the first draft of manuscript. TN, MT, and HS contributed integrations of NIRAS system and discussed analysis method. PD contributed discussion of NIRAS results at Kiruna. PD, YO, and UB contributed NIRAS installation at Kiruna and help its operation. TS was involved in this research and discussions. All authors contributed improving the manuscript. All authors have read and approved the final manuscript.

Funding
The NIRAS was funded by Japan Society for the Promotion of Science (JSPS), Grants-in-Aid for Young Scientists (A) 17H04857 and Scientific Research (B) 20H01962. It was also partly funded by Shimadzu Science Foundation, the prioritized project AJ0901 of Japanese Antarctic Research Expedition, and the Project Research KP301 of the National Institute of Polar Research.

Availability of data and materials
The NIRAS data can be accessed at "http://polaris.nipr.ac.jp/~nishiyama/#!data.md". Observed aurora spectrum data can be provided based on requests. Aura/MLS temperature and geopotential height data are from "https://acdisc.gesdisc.eosdis.nasa.gov/data/Aura_MLS_Level2/ML2T.005/2018/" and "https://acdisc.gesdisc.eosdisc.eosdis.nasa.gov/data/Aura_MLS_Level2/ML2GPH.005/2018/", respectively. NIPR fluxgate magnetometer data can be found at "https://scidbase.nipr.ac.jp/modules/metadata/index.php?content_id=102". All-sky aurora image data for Syowa can be found at "https://scidbase.nipr.ac.jp/modules/metadata/index.php?content_id=101". All-sky aurora image data for Kiruna can be found at "https://scidbase.nipr.ac.jp/modules/metadata/index.php?content_id=224". *K*-index data at Syowa is from "http://polaris.nipr.ac.jp/~aurora/syowa.magne/k-index/each.year/K2018.txt". *K*-index data at Kiruna are found from "https://www.irf.se/en/about-irf/data/" or "http://www2.irf.se//Observatory/k-index/". All-sky aurora image data for Sodankylä can be found at "https://www.sgo.fi/".

Ethics approval and consent to participate
Not applicable.

Consent for publication
Not applicable.

Competing interests
The authors declare that they have no competing interests.

Author details
[1] National Institute of Polar Research, 10-3, Midori-cho, Tachikawa, Tokyo 190-8518, Japan. [2] Department of Polar Science, The Graduate University for Advanced Studies, SOKENDAI, 10-3, Midori-cho, Tachikawa, Tokyo 190-8518, Japan. [3] Rikkyo University, 3-34-1, Nishi-Ikebukuro, Toshima-ward, Tokyo 171-8501, Japan. [4] Meiji University, 1-1-1, Higashi-Mita, Tama-ward, Kawasaki, Kanagawa 214-8571, Japan. [5] The Swedish Institute of Space Physics, Box 812, SE-981 28 Kiruna, Sweden. [6] Joint Support-Center for Data Science Research, Research Organization of Information and Systems, 10-3, Midori-cho, Tachikawa, Tokyo 190-8518, Japan. [7] Tohoku University, 6-3, Aramaki-Aza-Aoba, Aoba-ward, Sendai, Miyagi 980-8578, Japan.

Received: 30 September 2020 Accepted: 15 January 2021
Published online: 29 January 2021

References

Azeem SMI, Sivjee GG, Won Y-I, Mutiso C (2007) Solar cycle signature and secular long-term trend in OH airglow temperature observations at South Pole, Antarctic. J Geophys Res Space Phys 112:A1. https://doi.org/10.1029/2005JA011475
Baker JD, Stair TA (1988) Rocket measurements of the altitude distributions of the hydroxyl airglow. Physica Scripta 37:611–622. https://doi.org/10.1088/0031-8949/37/4/021
Damiani A, Storini M, Laurenza M, Rafanelli C (2008) Solar particle effects on minor components of the Polar atmosphere. Ann Geophys 26:361–370. https://doi.org/10.5194/angeo-26-361-2008
Damiani A, Storini M, Santee ML, Wang S (2010) Variability of the nighttime OH layer and mesospheric ozone at high latitudes during northern winter: influence of meteorology. Atmos Chem Phys 21:10291–10303. https://doi.org/10.5194/acp-10-10291-2010
Dewan EM, Pendleton W, Grossbard N, Espy P (1992) Mesospheric OH airglow temperature fluctuations: a spectral analysis. Atmos Chem Phys 19:597–600. https://doi.org/10.1029/92GL00391
Espy PJ, Pendleton WR Jr, Sivjee GG, Fetrow MP (1987) Vibrational development of the N_2^+ Meinel Band System in the aurora. J Geophys Res Space Phys 92:11257–11261. https://doi.org/10.1029/JA092iA10p11257
Espy PJ, Hibbins RE, Jones GOL, Riggin DM, Fritts DC (2003) Rapid, large-scale temperature changes in the polar mesosphere and their relationship to

meridional flows. Geophys Res Lett. https://doi.org/10.1029/2002GL016452
French W, John R, Klekociuk AR (2011) Long-term trends in Antarctic winter hydroxyl temperatures. J Geophys Res Atmos. https://doi.org/10.1029/2011JD015731
Gattinger RL, Jones A Vallance (1973) N_2^+ Meinel Auroral Spectra in the 1.5μ m Region. Can J Phys 53:480–487. https://doi.org/10.1139/p73-036
Gattinger RL, Jones A Vallance (1981) Quantitative spectroscopy of the aurora. V. The spectrum of strong aurora between 10000 and 16000 Å. Can J Phys 51:287–291. https://doi.org/10.1139/p81-059
Grygalashvyly M, Sonnemann GR, Lübken F-J, Hartogh P, Berger U (2014) Hydroxyl layer: mean state and trends at midlatitudes. J Geophys Res Atmos 119:12391–12419. https://doi.org/10.1002/2014JD022094
Jackman CH, Marsh DR, Vitt FM, Roble RG, Randall CE, Bernath PF, Funke B, López-Puertas M, Versick S, Stiller GP, Tylka AJ, Fleming EL (2011) Northern Hemisphere atmospheric influence of the solar proton events and ground level enhancement in January 2005. Atmos Chem Phys 11:6153–6166. https://doi.org/10.5194/acp-11-6153-2011
Jones AV, Gattinger RL (1976) Quantitative spectroscopy of the aurora. IV. The spectrum of medium intensity aurora between 8800 Å and 11400 Å. Can J Phys 54:2128–2133. https://doi.org/10.1139/p76-251
Krassovsky VI, Shefov NN, Yarin VI (1962) Atlas of the airglow spectrum 3000–12400 Å. Planet Space Sci 9:883–915. https://doi.org/10.1016/0032-0633(62)90008-9
Meinel IAB (1950) OH emission bands in the spectrum of the night sky. Astrophys J 111:555. https://doi.org/10.1086/145296
Meriwether WJ (1975) High latitude airglow observations of correlated short-term fluctuations in the hydroxyl meinel 8–3 band intensity and rotational temperature. Planet Space Sci 8:1211–1221. https://doi.org/10.1016/0032-0633(75)90170-1
Mies HF (1974) Calculated vibrational transition probabilities of OH($X^2\Pi$). J Mol Spectrosc 53:150–188. https://doi.org/10.1016/0022-2852(74)90125-8
Mulligan FJ, Horgan DF, Galligan JG, Griffin EM (1995) Mesopause temperatures and integrated band brightnesses calculated from airglow OH emissions recorded at Maynooth (53.2° N, 6.4°W) during 1993. J Atmos Terr Phys 57:1623–1637. https://doi.org/10.1016/0021-9169(94)00133-9
Ogawa Y, Tanaka Y, Kadokura A, Hosokawa K, Ebihara Y, Motoba T, Gustavsson B, Brändström U, Sato Y, Oyama S, Ozaki M, Raita T, Sigernes F, Nozawa S, Shiokawa K, Kosch M, Kauristie K, Hall C, Suzuki S, Miyoshi Y, Gerrard A, Miyaoka H, Fujii R (2020) Development of low-cost multi-wavelength imager system for studies of aurora and airglow. Polar Sci 23:100501. https://doi.org/10.1016/j.polar.2019.100501
Omholt A (1957) The red and near-infra-red auroral spectrum. J Atmos Terr Phys 10:320–331. https://doi.org/10.1016/0021-9169(57)90131-9
Partamies N, Amm O, Kauristie K, Pulkkinen TI, Tanskanen E (2003) A pseudo-breakup observation: localized current wedge across the postmidnight auroral oval. J Geophys Res Space Phys 108:SIA 4-1-SIA 4-10. https://doi.org/10.1029/2002JA009276
Pautet P-D, Taylor MJ, Pendleton WR, Zhao Y, Yuan T, Esplin R, McLain D (2014) Advanced mesospheric temperature mapper for high-latitude airglow studies. Appl Opt 26:5934–5943. https://doi.org/10.1364/AO.53.005934
Pautet P-D, Taylor MJ, Snively JB, Solorio C (2018) Unexpected occurrence of mesospheric frontal gravity wave events over South Pole (90° S). J Geophys Res Atmos 123:160–173. https://doi.org/10.1002/2017JD027046
Pendleton WR Jr, Taylor MJ, Gardner LC (2000) Terdiurnal oscillations in OH Meinel rotational temperatures for fall conditions at northern mid-latitude sites. Geophys Res Lett 27:1799–1802. https://doi.org/10.1029/2000GL003744
Pertsev N, Perminov V (2008) Response of the mesopause airglow to solar activity inferred from measurements at Zvenigorod, Russia. Ann Geophys 26:1049–1056. https://doi.org/10.5194/angeo-26-1049-2008
Phillips F, Burns GB, French WJR, Williams PFB, Klekociuk AR, Lowe RP (2004) Determining rotational temperatures from the OH(8–3) band, and a comparison with OH(6–2) rotational temperatures at Davis, Antarctica. Ann Geophys 22:1549–1561. https://doi.org/10.5194/angeo-22-1549-2004
Picone JM, Hedin AE, Drob DP, Aikin AC (2002) NRLMSISE-00 empirical model of the atmosphere: statistical comparisons and scientific issues. J Geophys Res Space Phys 107(A12):1468. https://doi.org/10.1029/2002JA009430
Schmidt C, Höppner K, Bittner M (2013) A ground-based spectrometer equipped with an InGaAs array for routine observations of OH(3–1) rotational temperatures in the mesopause region. J Atmos Solar Terr Phys 102:125–139. https://doi.org/10.1016/j.jastp.2013.05.001
Shapiro AV, Rozanov E, Shapiro AI, Wang S, Egorova T, Schmutz W, Peter Th (2012) Signature of the 27-day solar rotation cycle in mesospheric OH and H_2O observed by the Aura Microwave Limb Sounder. Atmos Chem Phys 12:3181–3188. https://doi.org/10.5194/acp-12-3181-2012
Sigernes F, Shumilov N, Deehr CS, Nielsen KP, Svenøe T, Havnes O (2003) Hydroxyl rotational temperature record from the auroral station in Adventdalen, Svalbard (78° N, 15° E). J Geophys Res Space Phys. https://doi.org/10.1029/2001JA009023
Sivjee GG, Walterscheid RL (1994) Six-hour zonally symmetric tidal oscillations of the winter mesopause over the South Pole Station. Planet Space Sci 42:447–453. https://doi.org/10.1016/0032-0633(94)00085-9
Suzuki H, Taguchi M, Kanai Y, Takeyama N (2009) Fast spectrometer for ground-based observations of OH rotational temperature. Appl Opt 48:1119–1127. https://doi.org/10.1364/AO.48.001119
von Savigny C, Eichmann K-U, Llewellyn EJ, Bovensmann H, Burrows JP, Bittner M, Höppner K, Offermann D, Taylor MJ, Zhao Y, Steinbrecht W, Winkler P (2004) First near-global retrievals of OH rotational temperatures from satellite-based Meinel band emission measurements. Geophys Res Lett. https://doi.org/10.1029/2004GL020410
von Savigny C, McDade IC, Eichmann K-U, Burrows JP (2012) On the dependence of the OH* Meinel emission altitude on vibrational level: SCIAMACHY observations and model simulations. Atmos Chem Phys 12:8813–8828. https://doi.org/10.5194/acp-12-8813-2012
von Savigny C (2015) Variability of OH(3–1) emission altitude from 2003 to 2011: Long-term stability and universality of the emission rate-altitude relationship. J Atmos Solar Terr Phys 127:120–128. https://doi.org/10.1016/j.jastp.2015.02.001

Publisher's Note